RAL-TR-2000-023

PRECISION MEASUREMENT OF X-RAY LINE SPECTRA BY ENERGY DISPERSION IN A GAS MICROSTRIP DETECTOR

J.E. Bateman

Rutherford Appleton Laboratory, Chilton, Didcot, Oxon, OX11 0QX, U.K.

12 June 2000

Abstract

It is shown that when a gas microstrip detector (GMSD) is operated in such a way as to gain freedom from detector wall effects, the response of the detector to an x-ray line is stable and can be fitted reliably with a lognormal distribution function. The lognormal function permits the fitting of adjacent, overlapping x-ray lines with an accuracy in position of a few eV with an attendant penalty in the statistics required for a given precision in the amplitude measurement. Experimental data and montecarlo simulation data are presented to indicate the possible range of usefulness of this technique for energy-dependent x-ray line spectroscopy in applications (such as x-ray fluorescence analysis). The usefulness of the lognormal fits for detector studies is also noted.

1. Introduction

In analytical techniques such as X-ray Fluorescence Analysis (XFA) and X-ray Absorption Fine Structure (XAFS) the detected x-rays occur as distinct lines (emitted by the atoms under study). The analytical techniques depend on the identification of the line position (in wavelength of energy) and the quantification of the x-ray flux in each line. Operation in the wavelength domain offers very high potential resolution in wavelength at the expense of a very low sensitivity to the x-ray flux because of the small solid angle of a typical monochromator. In the energy domain much greater solid angle is possible but the line resolution is generally much poorer. The detector of choice is the cryogenic semiconductor (Ge or Si) detector which can give a FWHM energy resolution down to the order of 150eV and is widely used in materials analysis systems. The main disadvantages of this device are the complexity and cost of the cryostat necessary for operation. Technical limitations arise from the finite front contact thickness (which raises the useful threshold of operation to ≈1keV) and the slow amplifier time constants necessary to achieve the low noise (which limit the data capture rates to ≈100kHz). Gas counters have been largely superseded in this field due to their poor energy resolution. However, at low x-ray energies (<10keV) the operational flexibility inherent in the gas counter (e.g. the gas filling can be tailored to a given application, internal counting can give "windowless" operation for very soft x-rays, etc.) has kept them alive in certain applications (e.g. the simpler XFA systems). The recent development of the Gas Microstrip Detector (GMSD) [1] has opened up new technical possibilities for gas detectors which are explored in this presentation.

2. The Gas Microstrip Detector

The GMSD consists of an array of fine metallic lines produced on a semiconducting glass substrate by standard micro-lithographic processes. Connected alternately to a high electrical potential (anodes and cathodes) the metal strips function as amplifiers of free electrons in the gas surrounding them. A drift cathode at a suitable distance from the plate (typically 10mm) defines the gas volume from which x-ray-induced electron clouds are collected onto the anodes for amplification. Gas gains of up to 5000 enable individual x-rays to be detected as a pulse in an amplifier connected to either a single strip or groups of strips. The practical importance of the GMSD technology is that all the high-resolution gain-defining elements are located on the glass plate which is now a simple component that can be cleaned, handled and connected up very simply. Further, the cylindrical geometry of the conventional proportional counter is replaced by planar geometry which is yet further simplified by the weak dependence of the gas gain on the drift electrode position [2]. A final advantage of the GMSD is its high rate capability. Using the divided electrode structure it is possible to achieve counting rate densities of ≈10MHz/cm^2, giving several tens of MHz for a typical detector area of several cm^2 [3].

3. X-ray Line Detection in the GMSD

The energy resolution achieved in a gas microstrip detector is determined by various factors but chiefly by the photoelectron and avalanche statistics [4] and varies with the x-ray energy approximately as $E_x^{1/2}$. Figure 1 (upper line) shows the pulse height

spectrum given by Mn K x-rays in a GMSD. The FWHM of the K_α peak (5.9keV) is 14.5%. This is a typical value for any well-constructed GMSD and it is difficult to make any significant improvement on this value in a practical detector [4]. As well as a central portion which is very approximately gaussian, the line response function (LRF) (i.e. the response of the detector to an x-ray line) of the GMSD has a long tail going down to zero energy. This tail is characteristic of all gas counters and is due to wall effects in which part of the electron cloud of an event is lost by collision with the wall or loss from the scavenged volume of the counter.

By constructing a GMSD in the form shown in figure 2 one can eliminate the low energy tail of the LRF [4]. In figure 2 the x-rays enter the drift space of the GMSD parallel to the plate and are collimated sufficiently well to prevent any x-ray converting close to the either the plate or the drift electrode (≈1mm). A central part of the plate is used as the main signal source and a section of plate on either side is used as a guard structure to veto events in which charge has been shared between the central section and a guard section. If the threshold on the guard sections is sufficiently low (<20% of the peak energy) this eliminates the "tail" events almost completely as the lower curve in figure 1 (red line) illustrates. The resulting PSF is little narrower in its core shape but it has now become relatively symmetric function, which is fitted rather well by a lognormal curve. The lognormal distribution is such that the logarithms of the pulse heights are normally distributed. This mode of operation of the GMSD effectively makes a "wall-less" counter.

The shape of the core LRF in a gas counter is generally assumed to be a normal distribution. This is in fact not the case. The effects of avalanche statistics, of electron loss to negative ion formation in the drift and non-homogeneity in the electric field all contribute to give the LRF a positive skew [4]. A particular property of the lognormal (LN) distribution is that it generates a positive skew which is dependent only on the single parameter σ_R the standard deviation (SD) of the logarithimic transform of the pulse height (PH) distribution. This parameter is notated as σ_R because it represents the relative resolution (SD/peak pulse height) of the PH spectrum. Thus 14.5% FWHM for Mn K_α transforms into σ_R=0.061.

The tests described below show that the LN distribution appears to give a stable representation of the LRF over a practical range of bias conditions for a typical GMSD.

4. Lognormal Fits to Mn X-ray Lines

The radioactive (internal conversion) x-ray source ^{55}Fe yields the Mn K_α and K_β lines at 5.9keV and 6.49keV. The relative intensity of the two lines can vary depending on the effect of differential absorption in the source, detector window and detector volume, but the K_β is generally found to be ≈20% of the total rate. In a detector filled with argon, a reflection of the two peaks appears at 2.9keV and 3.49keV due to the escape of the argon K x-rays from the counter volume without conversion. This provides a useful set of four lines (we neglect the presence of the Ar K_β in the escape spectrum) for calibrating the energy response of the detector. Figure 3 shows a PH spectrum of the Mn x-rays in a GMSD filled with argon +25% isobutane. The anti-

coincidence circuits are in operation with a threshold of 590eV giving a very clean spectrum containing ≈5x10^5 events.

Clearly the energy resolution of the GMSD (855eV FWHM) is inadequate to resolve the Mn K_β from the Mn K_α peak (separation 590eV); however, as figure 3 shows the sum of two LN distributions fits very well to the data and a further pair of LN distributions fit the Ar escape peaks equally well. Figure 4 plots the channel positions obtained from the fits against the known energies of the Mn lines. The K_α peaks have the best statistics, so they are used to generate the straight line fit. All four points lie close to the straight line fit.

A spectral line has only two innate properties, its amplitude and its position (we assume that any broadening due to atomic processes is negligible). These are represented by the parameters *a* and *c* in the formula for the LN distribution (equation (1)). The parameter *b* is the relative SD of the detector LRF (actually the SD of the normal curve in ln(x) space) which determines both the width and skewness of the distribution.

$$\frac{dn}{dx} = \frac{a}{\sqrt{2\pi}bx}\exp\left(\frac{(\ln(x)-\ln(c))^2}{2b^2}\right) \quad (1)$$

The errors dictated by the statistical noise are evaluated by the Marquart-Levenburg fitting routine and displayed in figure 3. (The Marquardt-Levenberg algorithm is used in the implementation in the commercial EasyPlot package [5].) The position errors are 0.097channels (2.2eV) in the K_α and 0.28ch (6.4eV) in the K_β. The amplitude errors are 2183 counts (in 3.63x10^5) for the K_α and 1972 counts (in 99439) for the K_β.

The relative SD of the LRF is assumed constant over the energy span of the K_α and K_β lines (0.59keV). One can allow the parameter *b* to fit separately to the K_β line but no significant improvement is seen. For the K_α line *b*=0.0606 giving a *FWHM* (2.36**b**100) of 14.3%. At the escape peaks *b*=0.091 giving a *FWHM* of 21.5% showing the typical increase of the relative LRF width as the x-ray energy decreases.

5. Lognormal Fits to High Energy X-ray Lines

"Wall-less" operation of the GMSD greatly enhances the pulse height spectra obtainable when high energy x-rays are detected. Figure 5 shows the spectrum obtained from an ^{241}Am fluorescence x-ray source with the silver target exposed. Fitting and subtracting the background scatter from the housing leaves two very clear groups of x-ray lines – the Ag K lines with their escapes and the Ni/Fe/Cr lines from the stainless steel housing with their escapes. In spite of the very poor statistics satisfactory fits can be obtained with the LN function as the plot of the peak channel versus the x-ray line energy shows (figure 6). The energy resolution (*b*) is held constant within each of the two groups of lines in the fits of figure 5.

Measurements of the relative FWHM using the range of x-ray energies available from the fluorescence source (Cu, Rb, Mo and Ag K) lines [4] show that:

$$FWHM = \sqrt{\frac{1061.5}{E_x} + 5.14^2} \ \% \qquad (2)$$

This expression shows the typical statistical behaviour with an additional 5.14% (2.3%R.M.S.) which represents (mostly) the fluctuation of the GMSD gain over the active area. The calibration of the LRF width can be used either to give the starting value of a three parameter fit to each peak or to remove one parameter and fit only the position and amplitude.

6. Application of Lognormal Fits to Detector Studies

The Mn K lines from the ^{55}Fe radioactive source are routinely used as a convenient test stimulus for x-ray detectors. The ability of the LN fits to resolve the K_α and K_β lines now gives a new level of precision in studying the energy resolution of the GMSD. Figure 7 compares the plots of the *FWHM* measured in the conventional way and by means of a LN fit ($236\sigma_R$) to the two lines as a function of the drift potential (V_d) in the set-up of figure 2 filled with argon + 25% isobutane. The characteristic feature of an optimum FWHM [4] (at around Vd=-1200V) is reproduced in both cases with the LN value approximately 1% lower than the conventional one.

This improvement is entirely due to the separation of the K_α and K_β lines which the LN fitting effects. Simulating the two line spectra with two LN distributions of the appropriate relative intensity and calculating the *FWHM* (conventionally defined) as the resolution of the LN is increased yields the plot seen in figure 8. Here the conventional measure of the *FWHM* is seen to rise to a fairly constant ≈2% greater than $236\sigma_R$ as the resolution deteriorates above 10% (the approximate separation of the two lines). In the case of an isolated line the conventional definition of the *FWHM* always exactly equals $236\sigma_R$. Thus, with the typical energy resolution available from gas counters, the presence of the K_β line routinely causes a significant overestimate of the counter resolution. Being skewed, the peak position (mode) of the LN distribution does not coincide with the centroid, so that even for an isolated line there is a small systematic error in using the peak value. In the case of two lines close together, such as the Mn K lines, the mode shows a small systematic movement as the detector resolution changes (figure 8).

The degradation of the *FWHM* seen in figure 7 as the drift field increases above the optimum has been analysed elsewhere [4] and shown to be due to an increased skewing of the PH distribution due to inhomogeneity in the paths followed by the x-ray-generated photoelectrons to the anode. The increased skewing reveals itself in a failure of the LN curve to match the experimental LRF and a systematic error in the position of the K_β line as evaluated by the LN fits. Figure 9 shows the fitted line positions of the four lines identifiable in the ^{55}Fe spectrum in an argon gas mixture with V_d=-1200V and V_d=-3000V. Apart from the extra gain caused by the higher V_d the fitted K_β line positions are (unlike the V_d=-1200V case) significantly in error with the line fitted to the K_α positions. Plotting this error as a function of V_d shows (figure 10) that beyond a V_d of ≈1200V the error increases rapidly as the LRF distorts from the LN shape.

A further diagnostic available from the fitting procedure is the relative intensity of the K_β and K_α lines. While the relative intensity is basically defined by the transition probabilities in the Mn atom, absorption in the source and detector window and differential efficiency in the detector do modulate the value. However, in a given experimental configuration the fraction of the K_β counts should remain a constant fraction of the total. Figure 11 shows this fraction plotted as a function of V_d. Between 1100V and 1500V this fraction remains constant (within the statistical errors) at ≈0.22.

It is clear from the data presented in figures 7,10 and 11 that for an argon + 25% isobutane gas mixture there is an ideal operating region of 1100V <-V_d < 1300V in which the detector is capable of resolving the Mn K_α and K_β lines with excellent energy resolution and proportionality.

7. Quantitation

In the fitted parameters of figure 3 two points are immediately noticeable; the position errors are very low, and the amplitude errors are high compared with the Poisson errors expected from the amplitudes i.e. 602 for K_α and 100 for K_β ($\sqrt{N}$). The factor of 3.63 increase in the SD of the fitted K_α means that 13.1 (3.63^2) times the number of counts must be collected to achieve the same amplitude resolution as would be achieved by a given number of events in the peak as detected by an ideal detector. The corresponding factor in the K_β case is 39.1. The ratio of the observed variance in the fitted number of counts to the Poisson value (i.e. σ_N^2/N) is known as the excess noise factor (F) and it represents the factor by which the counting time must be extended to achieve the same resolution in the counts as would be achieved by an ideal detector counting N events.

For a pair of closely spaced x-ray lines the excess noise factor (F) of each line fit is a function of $\alpha = \sigma_E/\delta E$, ($\sigma_E = \sigma_R E$ is the energy resolution of the LRF in keV) at the mean line position and δE is the energy spacing between the lines (in keV)) and the partition fraction between the two lines (f_p). Since setting up a range of x-ray lines with close (and variable) spacing is a large undertaking it was decided to explore the dependence of F on α and f_p by means of a montecarlo model. With the energy of the lower line set to 5keV at which $\sigma_R = 0.08$ (from equation (2)) and a variable separation between the lines, LN pulse height distributions were simulated with 10^5 (N) events in the combined lines divided according to f_p (the fraction of the counts in the lower line). The Marquardt-Levenberg fitting procedure was used to evaluate the error in the number of counts in each line (σ_N) and F was evaluated using the relation, $F = 1 + \sigma_N^2/f_p N$.

Figure 12 shows the prediction of the model for the excess noise factors in two closely spaced lines as a function of α in the case of $f_p = 0.8$, the approximate value for the Mn K_α, K_β. The values of F measured experimentally (figure 3) for the Mn lines are superimposed for comparison. The fact that the experimental values are approximately twice as bad as the model values probably reflects the fact that the model can only include the strictly stochastic effects and not any contributions from

such factors as an imperfect match between the experimental LRF and the LN distribution.

Figure 13 illustrates the general behaviour of *F* for the lower line under the influence of the poissonian noise as predicted by the model. Generally, *F* rises steeply with α at all f_p and *F* minimises for all values at $f_p=0.5$. As expected, the largest values of *F* are obtained at low f_p (few counts in the line) and high α (poor resolution). The curves for the upper peak are essentially similar if $(1-f_p)$ is plotted on the abscissa, although in some corners of parameter space the asymmetry of the LN distribution produces small differences. Clearly, *F* tends to infinity as f_p tends to zero and $F=1$ at $f_p=1$.

The errors in the fitted line energies are very small: for example at α=0.6, f_p=0.8 (corresponding to the Mn lines) errors of 3.6eV and 9.6eV are predicted by the model which compare with the measured values of 2.2eV and 6.4eV (figure 3). Thus one can view the fitting process as one which transfers the position noise of the initial spectrum into amplitude noise in the fitted parameters.

The implication of the above analysis is that, over a useful range of situations, the overlapping PH distributions from adjacent x-ray lines can be separated by fitting lognormal LRFs to the experimental spectra from a GMSD adapted for "wall-less" operation. The extra energy resolution is obtained at the cost of a greatly increased statistical requirement. Taking the α value typical of the Mn lines (0.6) shows that the statistics must be increased by a factor of between 5 and 100 to achieve the same amplitude resolution as an ideal detector for $0.1 < f_p < 0.9$. Alternatively, for a fixed number of counts the amplitude resolution is degraded by a factor of between 2.2 and 10. The line energy resolution is <10eV in this range of parameters.

The fitting algorithms run very fast on a 200MHz Pentium II processor: a few seconds for Marquardt-Levenberg and about 30 seconds for Downhill Simplex.

8. X-ray Fluorescent Analysis

An example of the possible application of this technique is x-ray fluorescent analysis (XFA). In XFA the ultimate requirement is (usually) to resolve the K lines of adjacent elements. Examining the separation between the K_α energies of adjacent elements (neglecting the presence of the K_β lines) one finds that it increases approximately as $E_K^{1/2}$. As equation (2) shows, the energy width of the LRF (σ_E) has a similar dependence on E_x so that in the case of adjacent K lines the parameter $\alpha=\sigma_E/\Delta E$ which determines the "separability" of lines is approximately constant. Figure 14 plots α for the case of separating adjacent K_α lines as a function of E_K (for the lower line) throughout the periodic table. As can be seen, α is relatively constant at ≈0.65 for adjacent elements and ≈0.33 for next-but-one elements.

Thus for adjacent K lines the values of F predicted for the fitting process lie just above the α=0.6 curve in figure 13. In other words for situations in which the weaker line contains at least 10% of the counts, one requires to accumulate between 10 and 200 times as many counts as would be required with an ideal detector in order to effect the separation to the same statistical precision.

9. Conclusions

The results described in this report may be summarised as follows.

- "Wall-less" operation of a GMSD with an argon/isobutane gas filling yields (under appropriate bias conditions) a stable point spread function (LRF) in response to an x-ray line.

- This LRF can be modelled by a lognormal distribution to a high degree of accuracy which permits fitting of the amplitude and position of the overlapping pulse height distributions generated by closely spaced x-ray lines.

- This process permits the separation of the Mn K_α and K_β lines emitted by an ^{55}Fe x-ray source and enhances the use of this common test source in the characterisation of GMSDs.

- Experimental measurements and montecarlo modelling show that line energies can be established to within a precision of 10eV for a wide range of practical cases. The signal to noise ratio in the amplitudes of the fitted lines degrades as a function of the parameters α (= $\sigma_E/\delta E$ – the energy resolution over the line separation) and f_p (the fraction of the counts in a pair of lines which is in the line under consideration). The excess noise factor (F) measures the factor by which the statistics in the data set need to be increased to recover the poissonian errors.

- For adjacent K lines in the periodic table the value of α is approximately constant at ≈0.65. With this value the adjacent lines can be separated by fitting with a penalty of F≈10 until the fraction of events in the line (f_p) drops below 0.3 when it rises steeply reaching F≈200 at f_p=0.1.

- Since the GMSD is a high rate device and is contemplated for use in high intensity SR beams, it is anticipated that the demand for extra statistics will not prove a barrier to the application of this technique in many experiments.

- The separation of x-ray lines by the technique described operates perfectly well in the sub-keV energy region. In this domain the window layer on semiconductor detectors poses a real limitation to their usefulness. A GMSD with a thin plastic window can operate down to energies below the carbon edge at ≈300eV.

References

1. Oed, Nucl. Instr. & Meth. A263 (1988) 351-359

2. J.E. Bateman, J.F.Connolly, G.E.Derbyshire, D.M.Duxbury, J.Lipp, J.A.Mir, R. Stephenson, J.E.Simmons and E.J.Spill, Rutherford Laboratory Report, RAL-TR-1999-057, (http://www-dienst.rl.ac.uk/library/1999/tr/raltr-1999057.pdf)

3. J.E. Bateman, J.F. Connolly, G.E. Derbyshire, D.M. Duxbury, J. Lipp, J.A. Mir, R. Stephenson, J.E. Simmons and E.J. Spill, R.C.Farrow, B.R.Dobson and A.D.Smith,

Gas Microstrip X-ray Detectors for Applications in Synchrotron Radiation Experiments, Rutherford Appleton Laboratory Report, RAL-TR-1999-056, (http://www-dienst.rl.ac.uk/library/1999/tr/raltr-1999056.pdf) Presented at the International Workshop on Micro-Pattern Gas Detectors, Orsay, France, 28-30 June 1999.

4. J.E.Bateman, J F Connolly, D.M.Duxbury, G.E.Derbyshire, J.A.Mir, E.J.Spill and R.Stephenson, Energy Resolution in X-ray Detecting Gas Microstrip Detectors, to be published.

5. EasyPlot for Microsoft Windows V 4.0 by Spiral Software

Figure Captions

1. A comparison of the pulse height spectra obtained from a GMSD with and without the anti-coincidence circuits of figure 2 in operation.

2. A schematic diagram of the mode of operation of a GMSD which permits pulse height spectra from an effectively "wall-less" counter to be obtained.

3. A plot of a "wall-less" pulse height spectrum of a ^{55}Fe x-ray spectrum with the lognormal fits to the Mn lines and the Ar escape lines superimposed.

4. A plot of the centroid channel identified by the lognormal fits (figure 3) against the known energies of the x-ray lines.

5. The pulse height spectra obtained with "wall-less" operation from a silver fluorescence source of x-rays. The lognormal fits to the various groups of x-ray lines are shown after background subtraction.

6. A plot of the centroids of the lognormal fits to the various peaks in the pulse height spectrum (figure 5) plotted against the x-ray line energies emitted from the fluorescence source.

7. The relative *FWHM* (%) of the Mn K_α line as measured by the conventional method in a GMSD and also by means of a lognormal fit to a "wall-less" pulse height spectrum.

8. A plot of the *FWHM* measured for the Mn K_α line in the presence of the K_β line by the conventional method against the lognormal fit value. The presence of the K_β line causes the conventional method to overestimate the *FWHM* by a significant amount. The discrepancy between the mode of the pulse height distribution and the correct K_α position is also shown.

9. The LN fit centroids of the four lines in the 55Fe spectrum are plotted against the x-ray line energies for two different drift potentials (-1200V and –3000V). At high drift field the distortion of the LRF becomes significant.

10. A plot of the error induced in the fitted K_β line energy by high drift potentials (from plots such as figure 9).

11. The fraction of the fitted counts in the K_β line of the ^{55}Fe pulse height spectrum as a function of the drift potential in the GMSD.

12. The excess noise factor induced in the fitted amplitude values (counts) of the Mn K_α and K_β lines as a function of the parameter $\alpha = \sigma_E/\delta E$, as predicted by the montecarlo model. The experimental values derived from figure 3 are shown for comparison.

13. The predictions of the montecarlo model for the behaviour of the excess noise factor (F) induced in a fitted line intensity as a function of α and the fraction of counts in the line (f_p).

14. The parameter α for successive pairs of K_α fluorescence lines detected in a GMSD, plotted as a function of the energy of the lower line up to Cu in the periodic table. The values for second neighbours are also plotted.

FIGURE 1

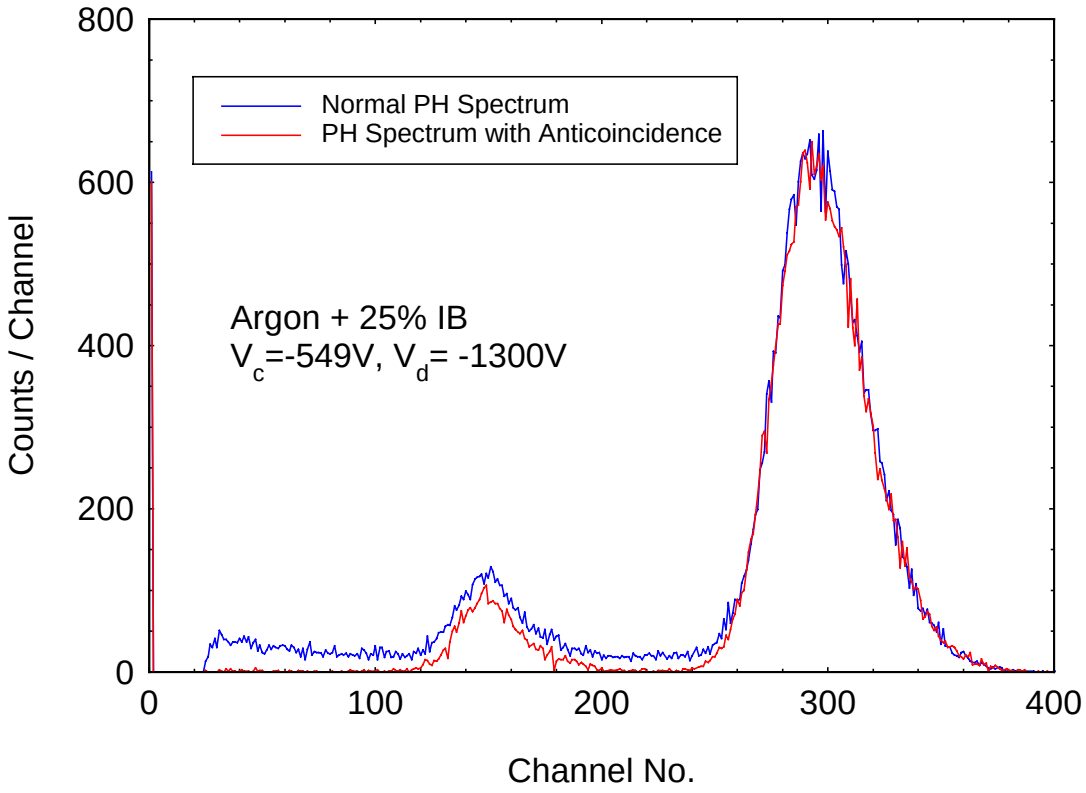

FIGURE 2

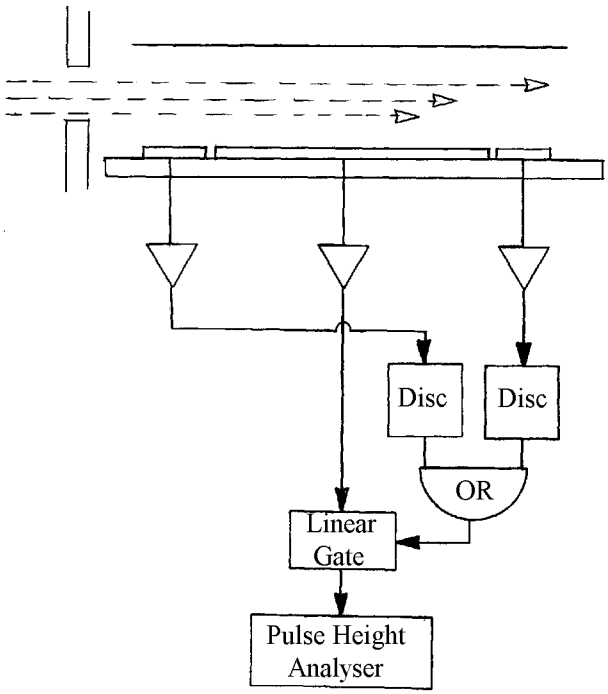

FIGURE 3

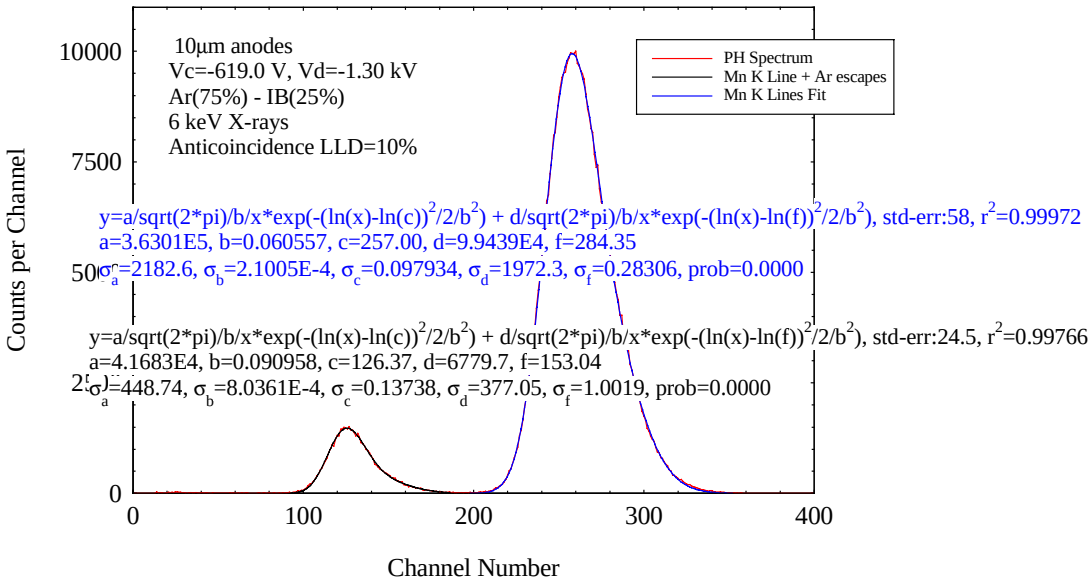

FIGURE 4

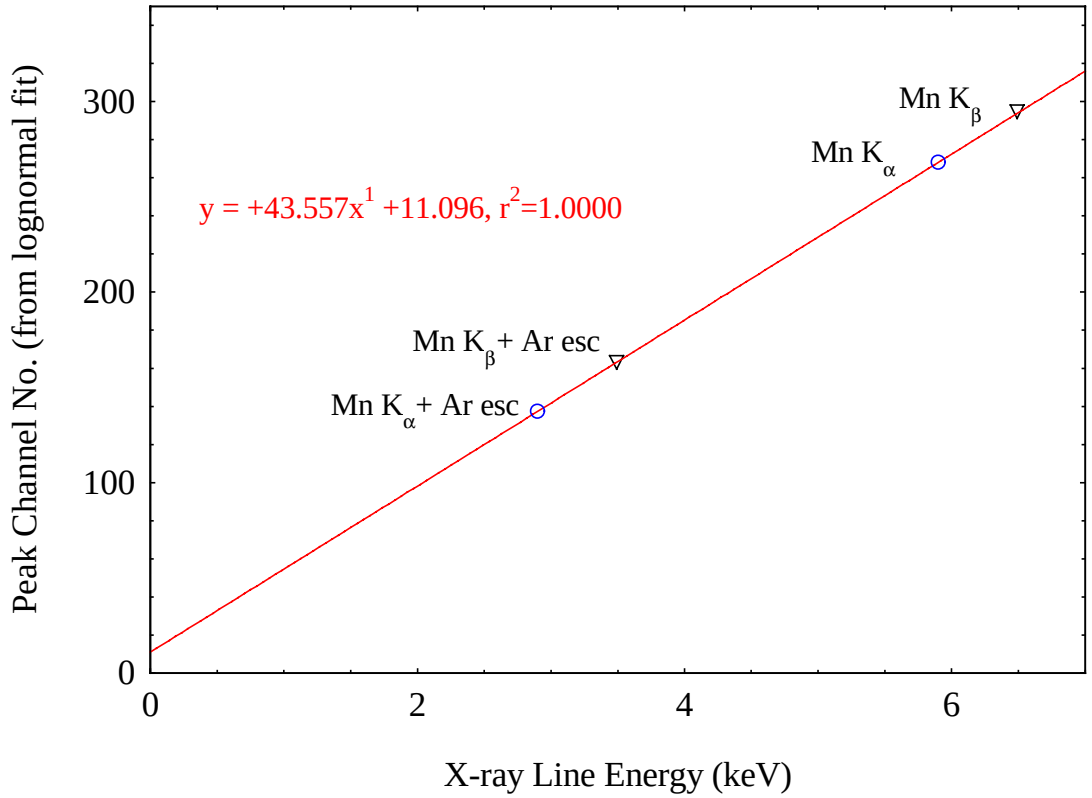

FIGURE 5

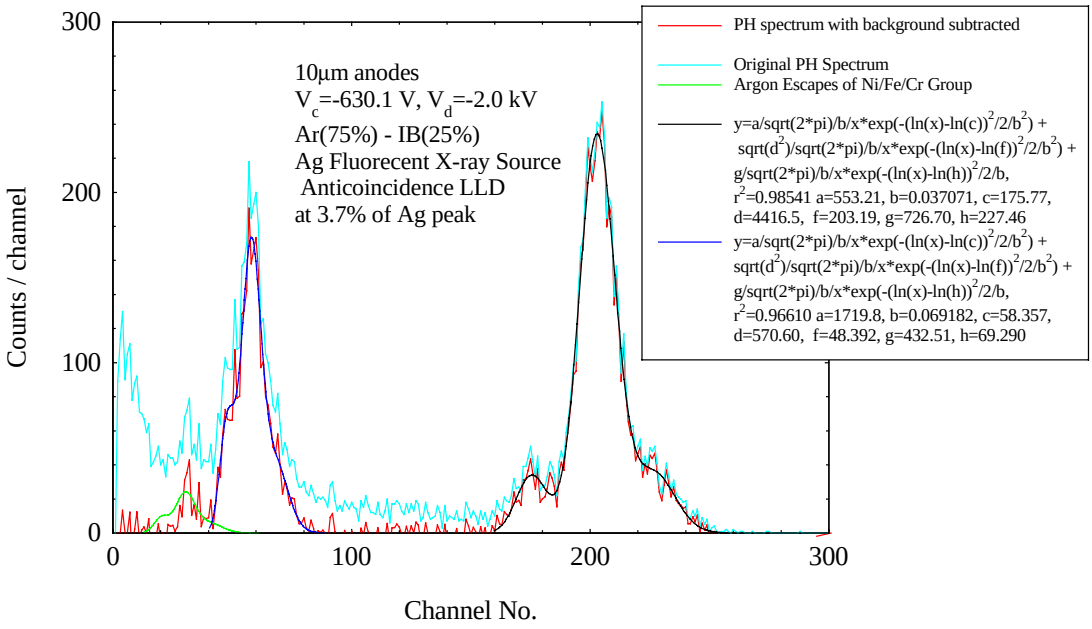

FIGURE 6

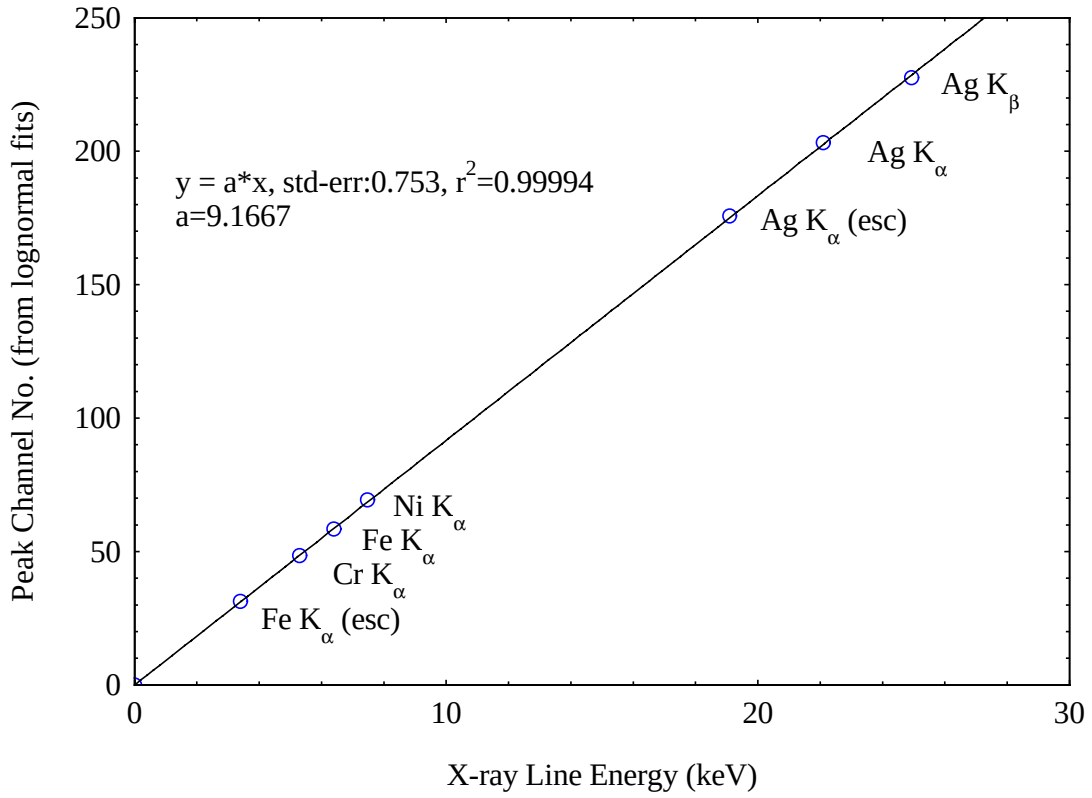

FIGURE 7

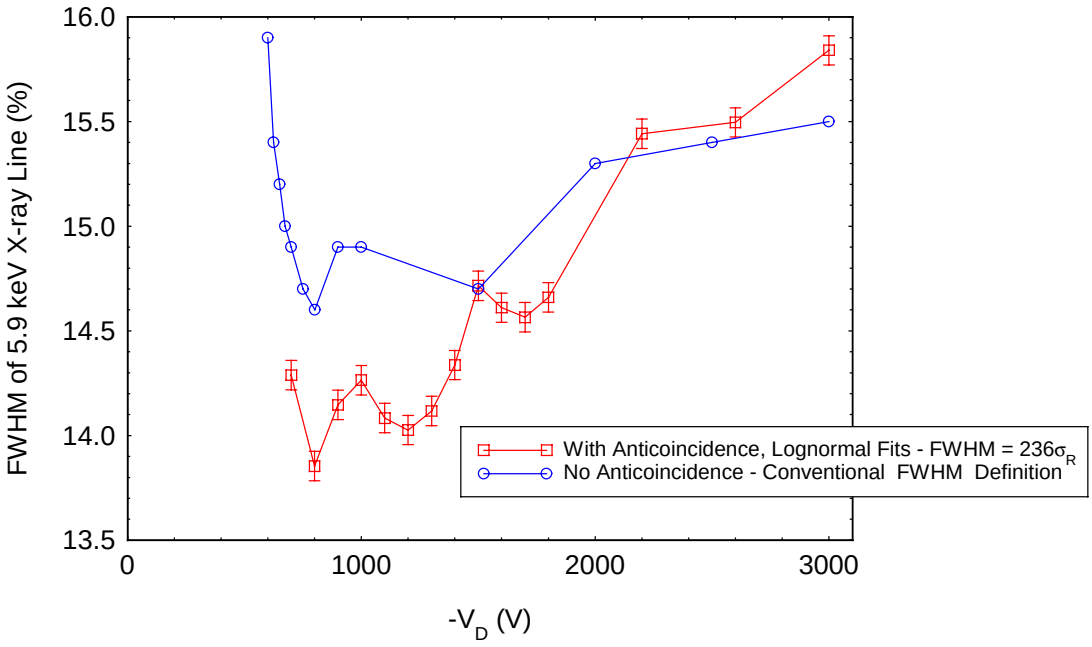

FIGURE 8

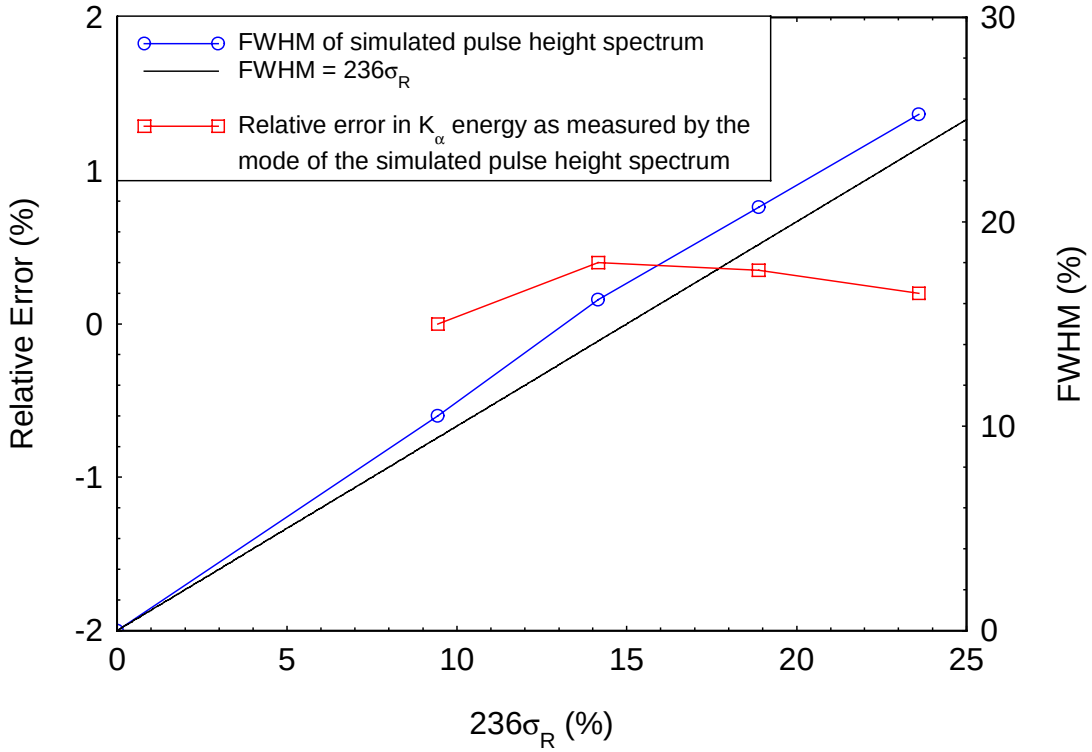

FIGURE 9

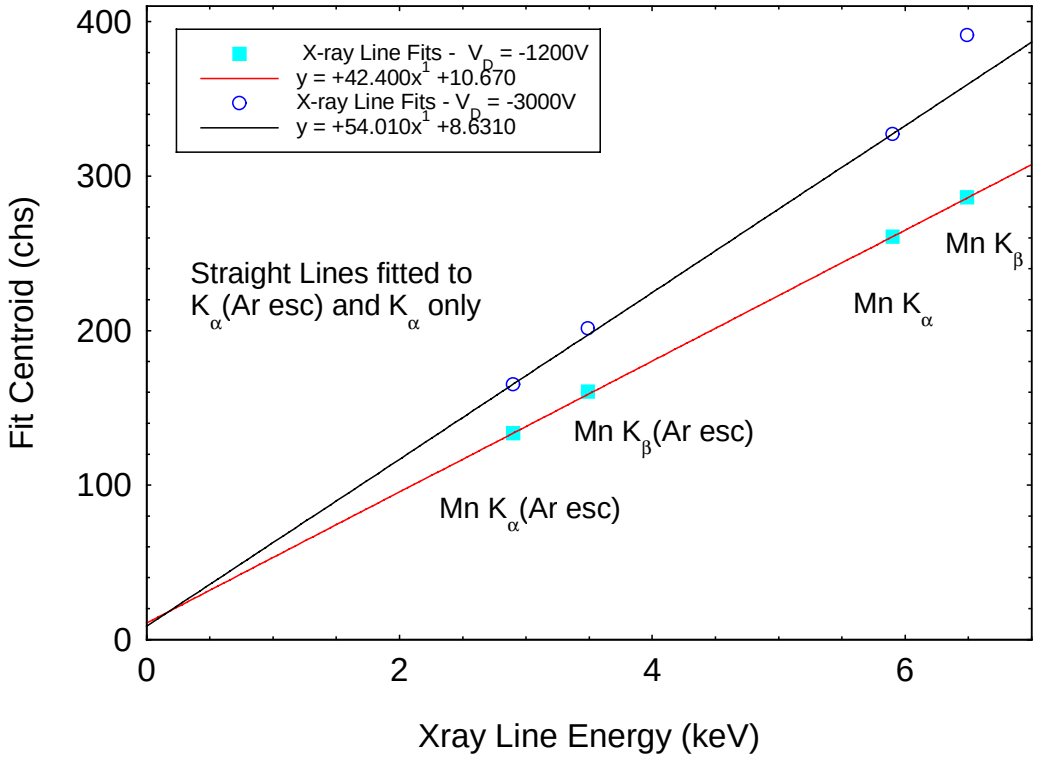

FIGURE 10

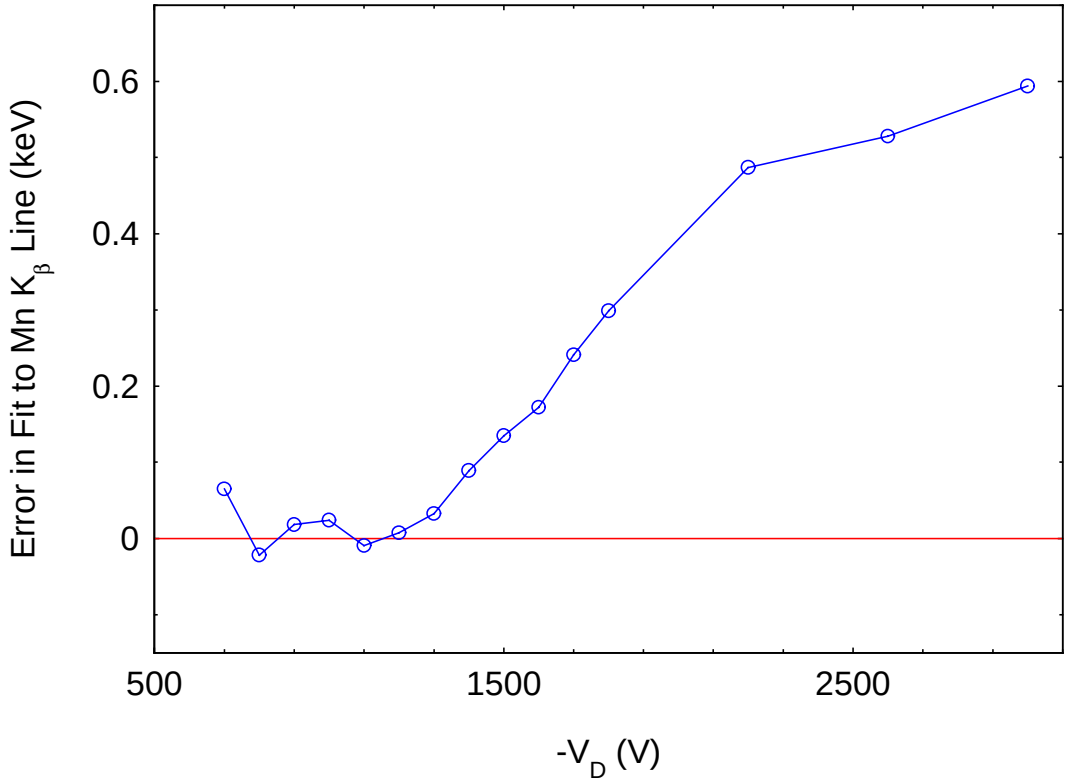

FIGURE 11

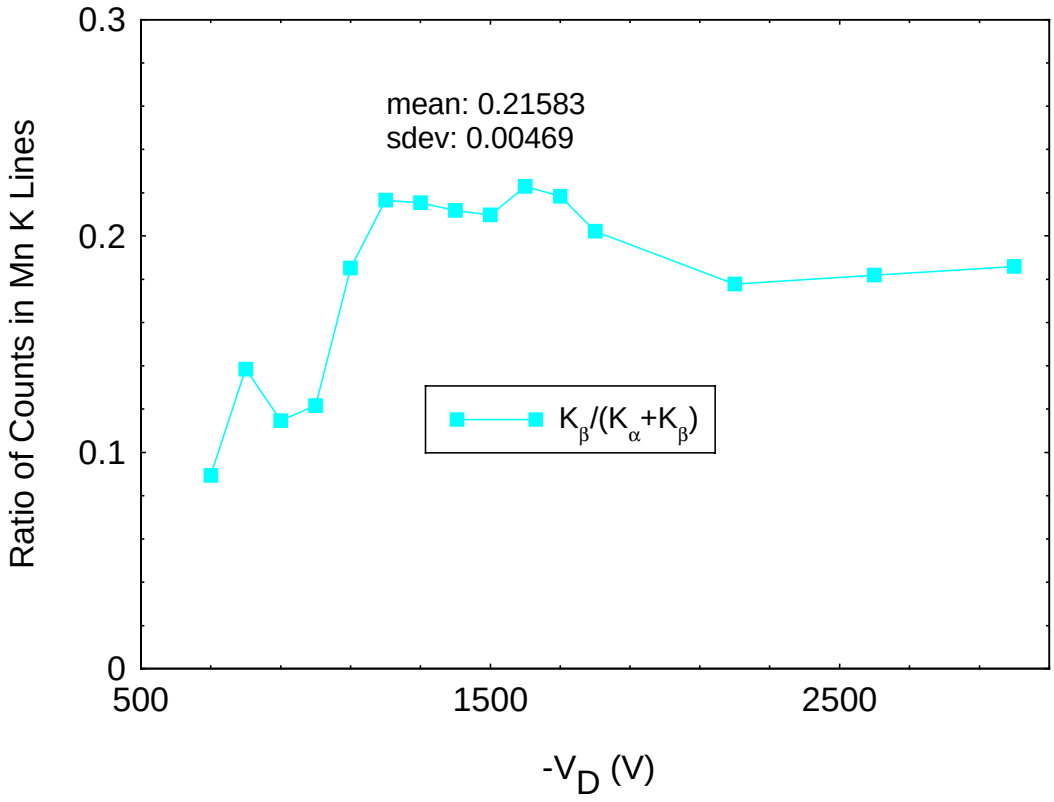

FIGURE 12

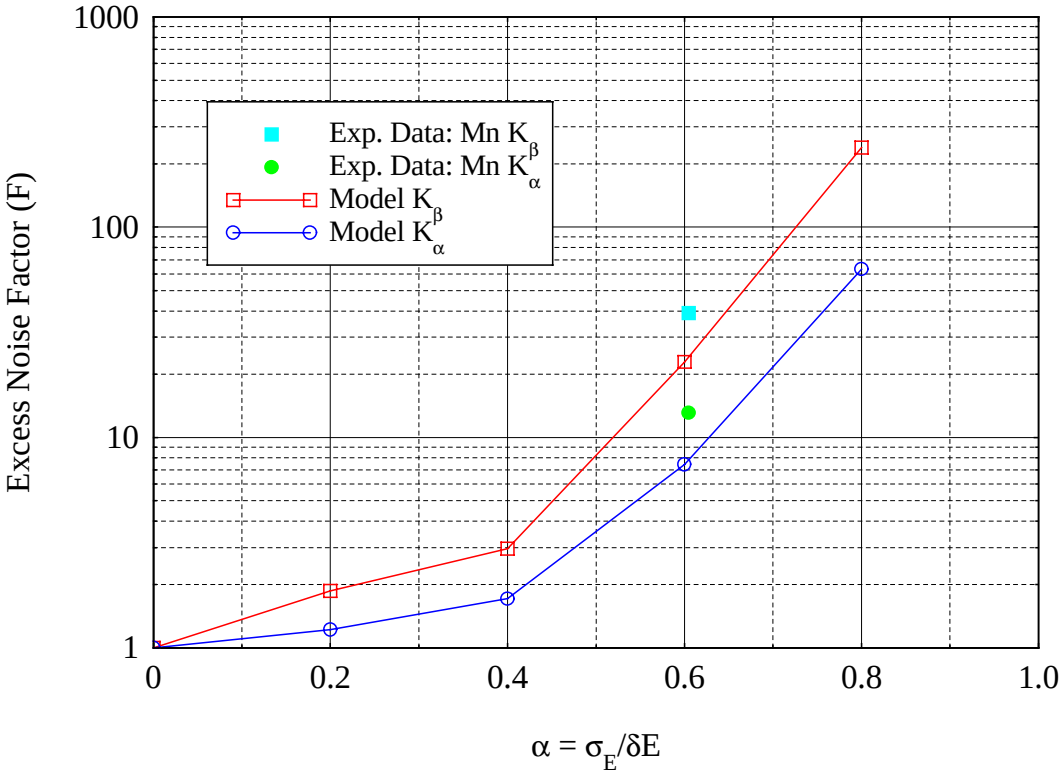

FIGURE 13

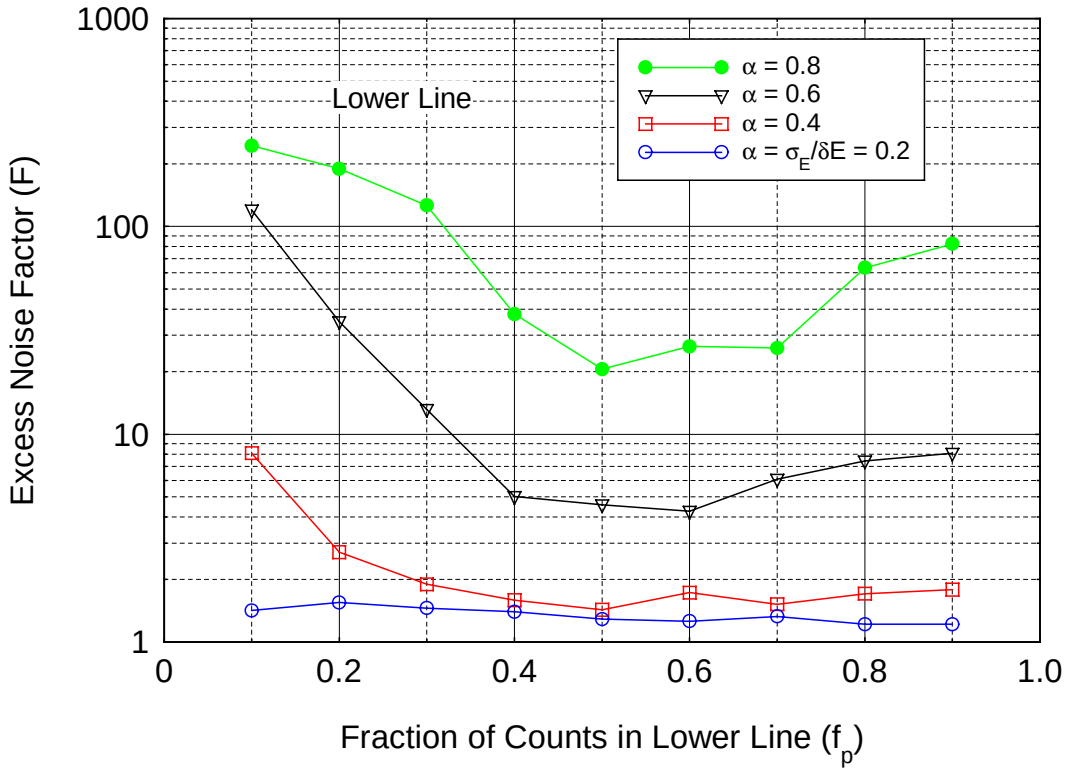

FIGURE 14